International Symposium
On Turbulence and Shear Flow
Phenomena (TSFP-9)
June 30 - July 3, 2015 *Melbourne, Australia*

USING EXPERIMENTAL OPTIMIZATION TO TUNE THE KINEMATICS OF A FLEXIBLE PROPULSOR

Daniel B. Quinn
Dept. of Mech. Engineering
Stanford University
Stanford, CA 94305, USA
dbq@stanford.edu

George V. Lauder
Dept. of Organismal and Evolutionary Biology
Harvard University
Cambridge, MA 02138, USA
glauder@oeb.harvard.edu

Alexander J. Smits[1,2]
[1]Dept. of Mechanical and Aerospace Engineering
Princeton University,
Princeton, NJ 08544, USA

[2]Department of Mechanical and Aerospace Engineering
Monash University
Melbourne VIC, Australia

ABSTRACT

Gradient-based optimization is used to maximize the propulsive efficiency of a heaving and pitching flexible panel. Random initial conditions are sequentially improved until a minimum step size is reached, at which point the condition is considered locally optimal. Optimum pitch and heave motions are found to produce nearly twice the efficiencies of optimum heave-only motions. Particle Image Velocimetry (PIV) is used to investigate the flow structures at optimal conditions. Efficiency is globally optimized when (1) the Strouhal number is within an optimal range that varies weakly with amplitude and boundary conditions; (2) the panel is actuated at a resonant frequency of the fluid-panel system; (3) heave amplitude is tuned such that trailing edge amplitude is maximized while the flow along the body remains attached; and (4) the maximum pitch angle and phase lag are chosen so that the effective angle of attack is minimized. The multi-dimensionality and multi-modality of the efficiency response demonstrate that experimental optimization appears to be well-suited for the design of flexible underwater propulsors.

INTRODUCTION

As first shown by Wu (1971), flexible propulsors can offer higher efficiencies than their rigid counterparts. These higher efficiencies are gathering increasing attention as advances in materials technology popularize flexible underwater vehicles, some of which can vary stiffness during operation (Park *et al.*, 2014). To isolate the effects of flexibility, most studies of flexible propulsors have considered either heave-only (Heathcote & Gursul, 2007; Michelin & Llewellyn Smith, 2009; Alben *et al.*, 2012; Quinn *et al.*, 2014) or pitch-only (Paulo *et al.*, 2011; Dai *et al.*, 2012; Dewey *et al.*, 2013; Raspa *et al.*, 2014) actuations at specific flow speeds or amplitudes. Here, we provide the first experimental investigation of flexible panels undergoing both heave and pitch over a range of of phase lags, amplitudes, and flow speeds.

To explore the full space of input parameters, we will use gradient-based optimization in addition to more traditional grid searches. One advantage of experimental optimization is that the analog nature of experimental techniques is combined with the rapidity of computational optimization. We show that optimization is especially well-suited for flexible propulsors, where achieving resonance requires particular combinations of input parameters that are unknown a priori. In addition to the optimization, we investigate the causes of the maximal efficiencies by considering select subspaces of the input parameters and conducting Particle Image Velocimetry (PIV) on a sample of near-optimal cases. This analysis helps to quantify the sensitivity of the optima to input conditions.

METHODS

Experiments were conducted on a flexible rectangular panel suspended in a free-surface recirculating water channel with flow speed u. The test section of the channel measured 0.26 m wide, 0.26 m deep, and 0.80 m long. Whenever possible, the surface of the water downstream of the panel was covered with a planar baffle to reduce surface waves, and the flow was conditioned upstream of the test section using angled baffles. The chord c, span s, thickness δ, and bending stiffness b of the panel were 195 mm, 150 mm, 0.11 mm, and $6.9*10^{-5}$ Nm^2, respectively. The leading edge of the panel was actuated with a lateral position h and angle of attack α that followed $h = a\sin(2\pi ft)$ and $\alpha = \alpha_0 \sin(2\pi ft - \phi)$, where a is the heave amplitude, α_0 is the maximum pitch angle, f is the frequency of oscillation, t is time, and ϕ is the phase lag between heave and pitch. The remainder of the panel deformed passively, producing

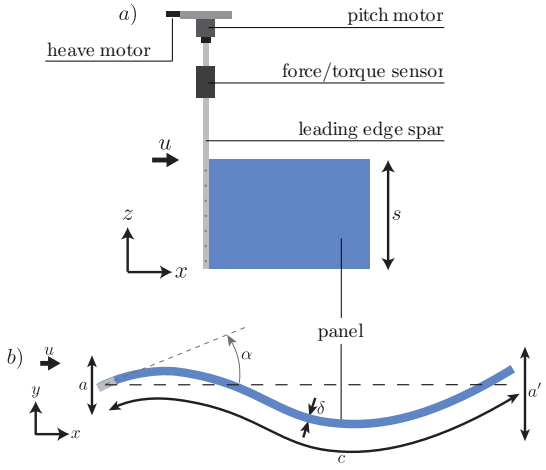

Figure 1. Experimental setup and length definitions. a: side view; b: top view.

a net streamwise force upstream at sufficient frequencies. A schematic of the setup is shown in figure 1.

A force-torque sensor was used to measure time-averaged streamwise force $\bar{\tau}$ and net power input to the fluid $\bar{\wp}$. Of particular importance to swimming performance is the propulsive efficiency $\eta \equiv \bar{\tau}u/\bar{\wp}$, which represents the fraction of useful energy transmitted to the surrounding flow. A grid search of the full input space was prohibitively time-intensive, so an optimization routine was used instead. Because the efficiency manifold is assumed to be smooth, a gradient-based or "hill-climbing" routine was chosen, where the proposed solution was iteratively shifted in the estimated direction of the gradient in efficiency. To account for multiple local maxima, the routine was run as a series of local searches. The goal of this approach is to discover the position in state space which maximizes $\eta(f,u,a,\alpha_0\sin\phi,\alpha_0\cos\phi)$. Note that α_0 and ϕ were converted to rectilinear coordinates in the α_0-ϕ plane, that is, (α_0, ϕ)→($\alpha_0\sin\phi$, $\alpha_0\cos\phi$). This substitution was necessary to prevent the routine from erroneously omitting pitch entirely in cases where pitch was introduced at a disadvantageous phase offset.

During each iteration of the routine, four steps were taken in each dimension of the state space: two steps at half the nominal step size and two steps at double the nominal step size. The nominal step sizes began at $\Delta f = 0.1$ Hz, $\Delta u = 10$ mm/s, $\Delta a = 2$ mm, $\Delta(\alpha_0\sin\phi) = 5°$, and $\Delta(\alpha_0\cos\phi) = 5°$, values chosen after exploratory convergence tests of the algorithm. After all dimensions were considered, the steps that maximized efficiency were applied to the proposed solution. In addition, if a halved/doubled step size yielded higher efficiency, that halved/doubled size became the new nominal size. In this way, the search routine could accelerate/decelerate, significantly decreasing the search time and offering a quantifiable stop condition.

The stepping routine was first applied to an arbitrary initial condition, and then at every subsequent position until a minimum step size was reached. The minimum step sizes found to best ensure convergence (while maintaining sufficient resolution) were one quarter of the initial nominal step sizes. Fifteen initial conditions were chosen to ensure a variety of relative strengths between input values (table 1). The routine was implemented in MATLAB, and activated through a script node in Labview to facilitate transfer between the algorithm and the experimental apparatus. The length of the search varied based on the initial condition, but no experiment took more than 10 iterations, corresponding to a maximum of 8 hours per experiment.

Table 1. Initial positions in state space for the 15 optimization trials that converged on optima A_{hp} and B_{hp}.

Trial	f (Hz)	u (mm/s)	a (mm)	$\alpha_0\sin\phi$ (°)	$\alpha_0\cos\phi$ (°)
1	0.7	180	5.9	6.4	-3.0
2	0.8	220	7.8	-14.5	10.7
3	1	130	7.8	6.0	12.8
4	1	130	15.6	-5.1	14.1
5	1.2	40	15.6	0	0
6	1.4	180	11.7	-19.0	-12.2
7	1.5	30	15.6	-5.1	14.1
8	1.5	90	9.8	5.1	-14.1
9	1.9	90	9.8	5.1	-14.1
10	2	150	9.8	-5.1	14.1
11	2	150	9.8	5.1	-14.1
12	2	150	9.8	14.1	5.1
13	2	150	9.8	-14.1	-5.1
14	2.4	40	7.8	-14.1	-5.1
15	2.5	220	5.9	0	0

At several optimum and near-optimum conditions, two-dimensional time-resolved Particle Image Velocimetry (PIV) was conducted at the midspan. The laser sheet was generated by a continuous 10W argon-ion laser (Coherent, Innova 70-C), and the particles were hollow silver-coated glass beads with an average diameter of 12 μm. Images were taken at 250 Hz with 1024×1024 resolution (Photron, FASTCAM 1024 PCI). The velocity field was calculated using Davis 8.1.3, the spatial cross-correlation algorithm developed by LaVision Inc. (Stanislas *et al.*, 2005). Four passes with 50% overlap were conducted on the data: two with 64×64 pixel windows and two with 24×24. The resulting velocity field consisted of 86×86 vectors. Phase-averaged velocity fields were calculated using the same number of cycles as the time-averaged force data. The PIV images were also used to calculate trailing edge amplitude, which was taken to be the average difference between extrema of the trailing edge position.

RESULTS

The optimization routine was first tested on a subspace of heave-only motions ($\alpha_0 = 0$). The relevant dimensionless parameters are the heave-chord ratio $a^* \equiv a/c$, the Strouhal number $St \equiv 2af/c$, and the "flexural frequency" $f^* \equiv f/\hat{f}_1$, where $\hat{f}_1$ is the first harmonic frequency of the fluid-panel system, estimated to be $(b/(\rho sc^5))^{1/2}$ via linear beam theory. See Quinn *et al.* (2015) for more details.

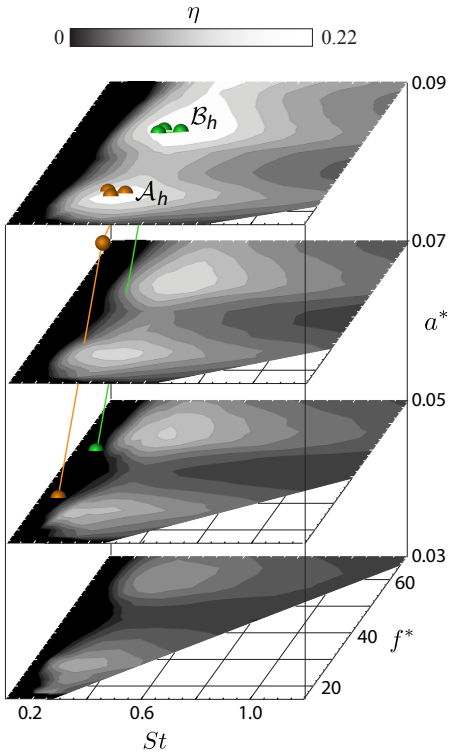

Figure 2. Contour plots of propulsive efficiency for heave-only motions. Colored lines show sample trajectories of the 3D optimization routine, terminating at optima A_h and B_h.

Whereas St compares the actuation frequency to time scales of the incoming flow, f^* relates the actuation frequency to time scales of fluid-structure resonance. With only three dimensions, a full grid search was possible, and figure 2 shows the efficiency manifold as a function of St, f^*, and a^*. The efficiency increased with increasing amplitude, presumably due to the lower relative contribution of viscous drag. Within constant a^* planes, however, a more complex η function is observed. Moving from low to high St at a fixed value of f^* shows the same sharp rise and slow taper commonly observed in rigid airfoil studies (Anderson *et al.*, 1998). Varying f^*, however, reveals a multimodal response in efficiency as the fluid-panel system passes through resonant modes. Within this heave-only space, global maxima in efficiency occur when heave amplitude is high and the optimum Strouhal number aligns with fluid-structure resonance. Figure 2 also shows the trajectory of two validation optimization routines, where the success of the routine is verifiable because the entire subspace has been mapped. Because of its initial condition, the routines discover only one of the two global optima, highlighting the need for multiple random-start local searches.

We now consider leading edge motions that include pitch, that is, where $\alpha_0 \neq 0$. Visualizing the trajectories of the routine is no longer trivial, and instead we show the efficiency at subsequent steps through the routines in figure 3. Each routine is characterized by a rapid rise in efficiency during the large initial steps of the routine, then a slow rise as the routine fine-tunes the parameters for optimum efficiency. As in the three-dimensional heave-only subspace, two distinct optima were discovered, representing two resonant modes of the fluid-panel system. Table 2 shows the average conditions in the two clusters to which the algorithm converged, as well as the conditions at the heave-only optima for comparison. The fact that the f^* values are relatively unchanged is evidence that these newly discovered optima are the same resonant modes as those observed in the heave-only case. The major changes between the two cases are: (1) the heave-only optima have higher St values, meaning the heave-only propulsors need to heave faster to achieve the same zero net thrust flow speed; (2) an equilibrium amplitude was reached in the trials with pitch ($a^* = 0.07$), suggesting that dynamic stall was a limiting factor in the five-dimensional optimization; and (3) introducing pitch nearly doubles the propulsive efficiencies.

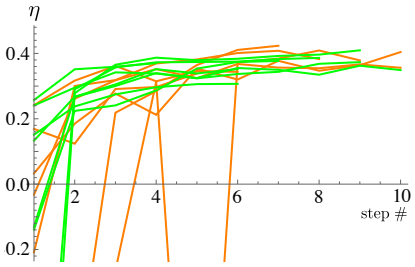

Figure 3. Efficiency at subsequent steps of the optimization routine. Orange lines show trajectories converging on A_{hp}; green lines show trajectories converging on B_{hp}.

Table 2. Input parameters and efficiencies at optimum conditions for heave-only motions (A_h and B_h) and heave/pitch motions (A_{hp} and B_{hp}).

Optimum	St	f^*	a^*	α	ϕ	η
A_h	0.40	27	0.09	-	-	0.21
B_h	0.53	57	0.09	-	-	0.23
A_{hp}	0.26	25	0.07	30°	76°	0.38
B_{hp}	0.33	51	0.07	30°	96°	0.37

After the optima were discovered, additional experiments were performed at optimal and near-optimal conditions. The first set of tests were done to explore the effects of phase offset, where efficiency was measured at optimal a^*, f^*, and St values, but non-optimal α_0 and ϕ values. Figure 4 shows the resulting efficiency contour plot in the ϕ-α_0 plane, and it demonstrates that introducing pitch is not always advantageous. For some values of ϕ, introducing pitch can decrease efficiency, and can even push the propulsor into a drag-producing regime. The phase at B_{hp} is indistinguishable from 90° within the experimental error. This condition corresponds to the minimum effective angle of attack, and is consistent with linearized models of propulsive panels (Lighthill, 1970). As a demonstration, figure 4 also shows an optimization routine that uses α_0 and ϕ as input parameters rather than $\alpha\cos\phi$ and $\alpha\sin\phi$. As noted in the methods section, this substitution causes the routine to get stuck at $\alpha_0 = 0$, because it starts at a phase offset where adding pitch had a negative effect.

Figures 2 and 4 help to place the optimal conditions in the context of the larger parameter space. To understand

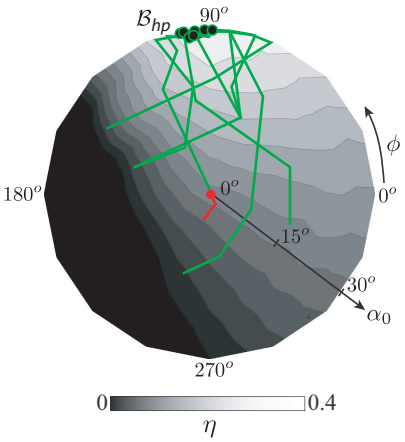

Figure 4. Contour plots of efficiency in the α_0-ϕ plane near $B_{\rm hp}$. Green lines: projections of trajectories of the 5D optimization routine, terminating in outlined circles near $B_{\rm hp}$. Red line: projection of a sample optimization trajectory where α and ϕ were used in place of $\alpha\cos\phi$ and $\alpha\sin\phi$.

the hydrodynamic reasons that certain conditions were optimal, we turn to Particle Image Velocimetry (PIV) taken at several sample conditions. All PIV data considered are phase-averaged snapshots of vorticity at the moment when the leading edge passes the y-axis headed toward negative y-values since this point best distinguishes the various cases. Figure 5 shows the flow field for optimum conditions $A_{\rm h}$ and $A_{\rm hp}$. Both flows are characterized by a thin layer of vorticity along the panel and a 2S reverse von Kármán street in the wake. The efficiency measurements, however, showed that $A_{\rm hp}$ demonstrates nearly double the efficiency of $A_{\rm h}$. A primary difference between the two cases is the presence of a leading edge vortex in $A_{\rm h}$ (figure 5*a*). It appears that by decreasing the effective angle of attack, the nonzero pitch angle reduces leading edge separation. Introducing pitch also leads to a lower Strouhal number at optimum conditions ($St = 0.26$ compared to to 0.40), which is known to be in the range of Strouhal numbers that optimize wake stability (Triantafyllou *et al.*, 1993). This feature is reflected by the greater coherence of the vortex street for $A_{\rm hp}$ (figure 5*b*).

To examine the effect of Strouhal number more closely, we consider perturbations from an optimum condition, this time from $B_{\rm h}$. Figure 6 shows the flow field at $B_{\rm h}$ as well as at non-optimal values of St and f^*. Strouhal numbers less than and greater than optimal will be referred to as St^- and St^+, respectively, and other parameters will follow the same convention. When St is lower than optimal (St^-, figure 6*b*), the wave along the body is too slow to keep pace with the incoming flow, and a large vortex detaches from the body just downstream of the first peak in lateral position. At St^+, no separation occurs along the body, but the vortices in the wake break down farther upstream. The thrust and power data confirm that these conditions are associated with lower efficiencies.

Variations in f^* lead to less significant differences in the flow field, as seen in figure 6*c*. The f^{*-} case shows the beginnings of a transition to a 2P wake, though this may be due more to the lower flow speed required to keep St constant when decreasing f^*. The more significant difference is believed to be the lower trailing edge amplitudes observed at non-optimal f^* values. Compared with $a'/a = 1.68$ at

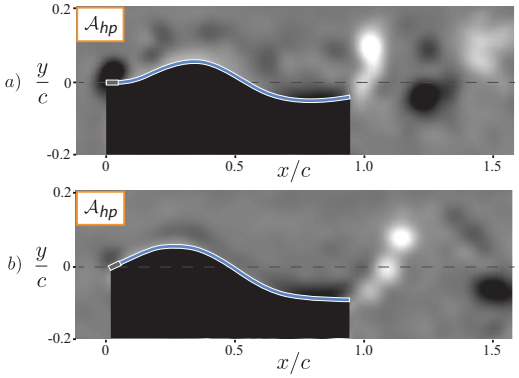

Figure 5. Phase-averaged density plots of vorticity: a: 1st optimum condition in the heave-only subspace ($A_{\rm h}$), $St = 0.40$, $f^* = 27.0$, $a^* = 0.09$; b: 1st optimum condition in the full parameter space ($A_{\rm hp}$), $St = 0.26$, $f^* = 24.8$, $a^* = 0.07$, $\alpha = 30°$, $\phi = 76°$.

$B_{\rm h}$, the low and high f^* conditions give $a'/a = 1.66$ and 1.52, respectively. At the same f^* values but with the flow speed fixed at its respective optimal value, the decreases were more pronounced, with $a'/a = 1.63$ and 1.51. An error analysis of the edge tracking technique suggests that ± 0.02 is a proper confidence interval for a'/a, so these decreases are significant. The zero in $\partial a'/\partial f^*$ at optimal conditions confirms that f^* is associated with resonance, and that the efficiency is locally maximized at resonant frequencies of the fluid-structure system.

Since the efficiency increases with a^* through the full space of a^* values (0.03 - 0.09), it may be more revealing to consider the effects of varying a^* around $B_{\rm hp}$, where the optimum a^* value was 0.07. Figure 7 shows the flow field at non-optimal values of a^*, as well as at non-optimal values of ϕ and α. For the a^* perturbations, flow speed was kept constant instead of St, because higher flow speeds reduce the amplitude along the body and interfere with conclusions about amplitude effects. In the case of a^{*+}, amplitudes higher than optimal lead to detached flow along the body. Presumably the lateral pressure gradients become sufficiently adverse for the boundary layer to separate from the panel. The a^{*-} case shows no such separation, while the optimal case shows the beginnings of separation. The efficiency data indicated that in this low amplitude regime, higher amplitudes are associated with higher efficiencies. It appears, therefore, that the efficiency is optimized when the amplitude is as high as possible but low enough for the flow to stay attached along the body.

Changing ϕ has severe consequences for the surrounding flow field (figure 7*c*, *d*). In the ϕ^- condition, the effective angle of attack is approximately twice what it is in the optimum condition, and the resulting periodic separation is evident to the side of the panel. In addition, heave and pitch are working against each other such that a'/a drops to 0.99 from 1.55 at $B_{\rm hp}$. The result is a severe drop-off in efficiency going counterclockwise from 90° in figure 4. In the ϕ^+ condition, heave and pitch are working constructively, a'/a increases to 2.01, and thrust is higher than in the $\phi = 90°$ case. As figure 4 shows, however, the higher effective angles of attack still cause lower efficiencies as ϕ increases beyond 90°, albeit at a slower rate than when ϕ is decreased. The result is that the optimum ϕ remains at 90°.

Finally, we consider variations in maximum pitch angle α_0. Since the pitch angle converged to the boundary of

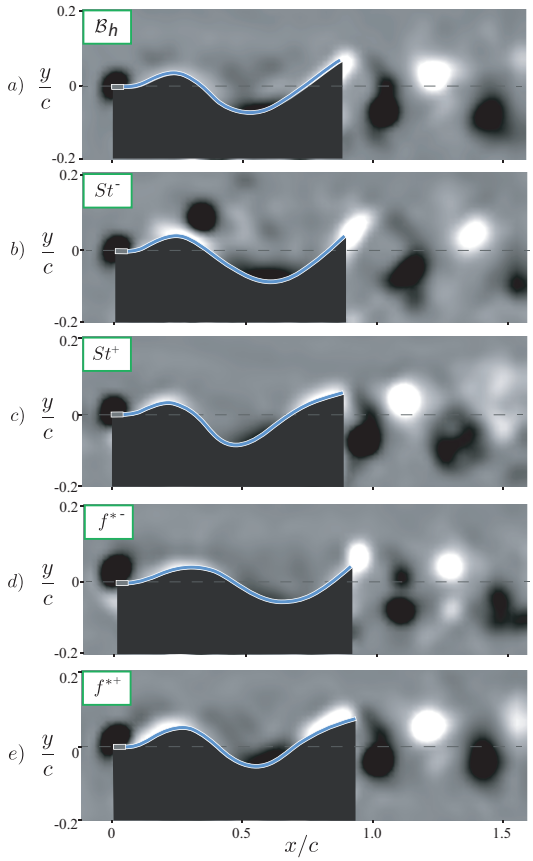

Figure 6. Phase-averaged density plots of vorticity: (a) 2nd optimum condition in the heave-only subspace (B_{h}), $St = 0.53$, $f^* = 56.8$, $a^* = 0.09$; (b, c) non-optimum St conditions near B_{h}, $St = 0.39$ for St^- and $St = 0.86$ for St^+; (d, e) non-optimum f^* conditions near B_{h}, $f^* = 44.6$ for f^{*-} and $f^* = 61.9$ for f^{*+}. All other variables were held at their optimum values. Vorticity scaling as in figure 5.

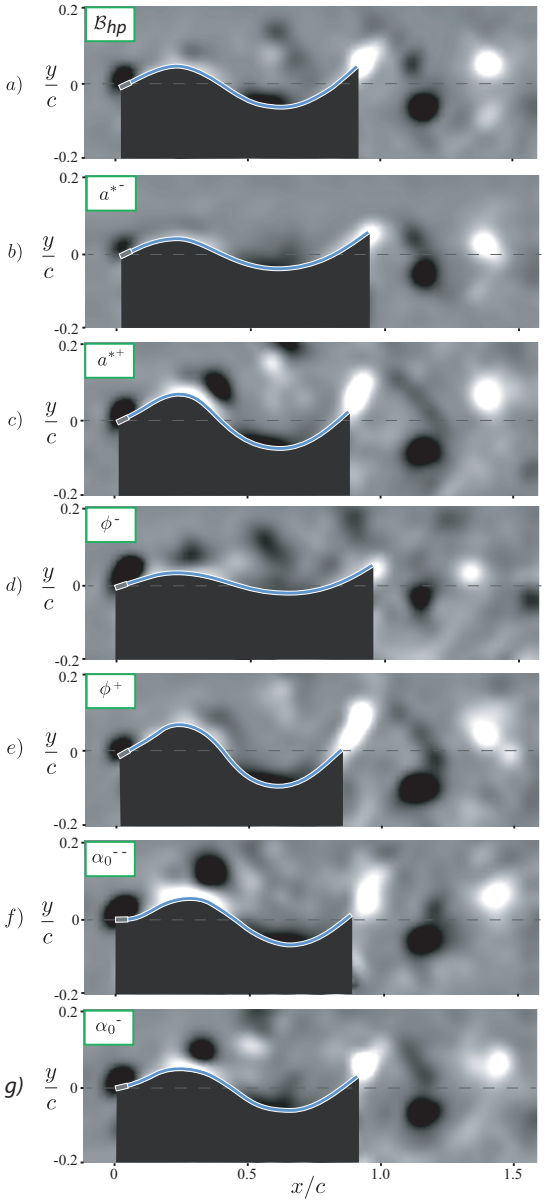

Figure 7. Phase-averaged density plots of vorticity: (a) 2nd optimum in the full parameter space (B_{hp}), $St = 0.33$, $f^* = 50.8$, $a^* = 0.07$, $\alpha = 30°$, $\phi = 96°$; (b, c) non-optimum a^* conditions near B_{hp}, $a^* = 0.05$ for a^{*-} and $a^* = 0.09$ for a^{*+}; (d, e) non-optimum ϕ conditions near B_{hp}, $\phi = 41°$ for ϕ^- and $\phi = 141°$ for ϕ^+; (f, g) non-optimum α conditions near B_{hp}, $\alpha = 15°$ for α^- and $\alpha = 0°$ for α^{--}. Vorticity scaling as in figure 5.

the range considered (30°), we use 15° (α^-) and 0° (α^{--}) as perturbed conditions. Both cases lead to increased separation along the panel, which is consistent with the fact that the effective angle of attack is increasing.

CONCLUSIONS

Direct force measurements and PIV suggest that propulsive efficiency is globally optimized when (1) the Strouhal number is high enough that the flow does not separate over peaks and troughs in the panel waveform, but low enough that the wake is stable and coherent, (2) the flexural frequency is one of a set of resonant frequencies of the fluid-panel system, (3) the heave-to-chord ratio is as high as possible, so long as the boundary layer along the body stays attached, (4) the max pitch angle is such that the effective angle of attack is minimized, thereby reducing separation at the leading edge, and (5) the phase lag between pitch and heave is 90°, or in some cases just less than 90°.

The multi-dimensionality and multi-modality of the efficiency space reveals that flexible propulsors are prime candidates for optimization routines. This study shows that even a simple gradient-based optimization can significantly improve the efficiency of a flexible panel. Optimizing the pitch and phase, for example, produced nearly double the best efficiencies of the heave-only case (0.38 compared with 0.23). The same routine could be applied to more complex three-dimensional propulsors with optimized planforms and an arbitrary number of kinematic inputs. Used in this way, experimental optimization would be a powerful tool for the design of flexible underwater vehicles.

Acknowledgments

This work was supported by the Office of Naval Research under MURI grant number N00014-08-1-0642 (Pro-

gram Director Dr. Bob Brizzolara), and the National Science Foundation under Grant DBI 1062052 (PI Lisa Fauci) and Grant EFRI-0938043 (PI George Lauder). The authors would also like to thank Patrick Thornycroft and Erik Anderson, who provided invaluable assistance in the automation of the experiment.

REFERENCES

Alben, S., Witt, C., Baker, T. V., Anderson, E. & Lauder, G. V. 2012 Dynamics of freely swimming flexible foils. *Phys. Fluids* **24** (051901).

Anderson, J. M., Streitlien, K., Barrett, D. S. & Triantafyllou, M. S. 1998 Oscillating foils of high propulsive efficiency. *J. Fluid Mech.* **360**, 41–72.

Dai, H., Luo, H., Paulo, J. S., Ferreira de Sousa, A. & Doyle, J. F. 2012 Thrust performance of a flexible low-aspect ratio pitching plate. *Phys. Fluids* **24** (101903).

Dewey, P. A., Boschitch, B.M., Moored, K. W., Stone, H.A. & Smits, A. J. 2013 Scaling laws for the thrust production of flexible pitching panels. *J. Fluid Mech.* **732**, 29–46.

Heathcote, S. & Gursul, I. 2007 Flexible flapping airfoil propulsion at low reynolds numbers. *AIAA* **45** (5), 1066–1079.

Lighthill, M. J. 1970 Aquatic animal propulsion of high hydromechanical efficiency. *J. Fluid Mech.* **44**, 265–301.

Michelin, S. & Llewellyn Smith, S. G. 2009 Resonance and propulsion performance of a heaving flexible wing. *Phys. Fluids* **21** (071902).

Park, Y. J., M., Huh T., Park, D. & Cho, K. J. 2014 Design of a variable-stiffness flapping mechanism for maximizing the thrust of a bio-inspired underwater robot. *Bioinspir. Biomim.* **9** (036002).

Paulo, J. S., Ferreira de Sousa, A. & Allen, J. J. 2011 Thrust efficiency of harmonically oscillating flexible flat plates. *J. Fluid Mech.* **674**, 43–66.

Quinn, D.B., Moored, K.W., Dewey, P.A. & Smits, A.J. 2014 Unsteady propulsion near a solid boundary. *J. Fluid Mech.* **742**, 152–170.

Quinn, D. B., Lauder, G. V. & Smits, A. J. 2015 Maximizing the efficiency of a flexible propulsor using experimental optimization. *J. Fluid Mech.* **767**.

Raspa, V., Ramananarivo, S., Thiria, B. & Godoy-Diana, R. 2014 Vortex-induced drag and the role of aspect ratio in undulatory swimmers. *Phys. Fluids* **26** (041701).

Stanislas, M., Okamoto, K., Kahler, C.J. & Westerweel, J. 2005 Main results of the second international piv challenge. *Exp. Fluids* **39**, 170–191.

Triantafyllou, G. S., Triantafyllou, M. S. & Grosenbaugh, M. A. 1993 Optimal thrust development in oscillating foils with application to fish propulsion. *J. Fluids & Struct.* **7**, 205–224.

Wu, T. Y. 1971 Hydrodynamics of swimming propulsion, part 1: swimming of a two-dimensional flexible plate at variable forward speeds in an inviscid fluid. *J. Fluid Mech.* **46** (2), 337–355.